

# A computational study on porosity evolution in parts produced by selective laser melting

Tan, Jie Lun; Tang, Chao; Wong, Chee How

2018

Tan, J. L., Tang, C. & Wong, C. H. (2018). A computational study on porosity evolution in parts produced by selective laser melting. Metallurgical and Materials Transactions A. <https://dx.doi.org/10.1007/s11661-018-4697-x>

<https://hdl.handle.net/10356/102487>

<https://doi.org/10.1007/s11661-018-4697-x>

---

© 2018 The Minerals, Metals & Materials Society and ASM International. All rights reserved.  
This paper was published by Springer in Metallurgical and Materials Transactions A and is made available with permission of The Minerals, Metals & Materials Society and ASM International.

*Downloaded on 13 Mar 2024 16:11:00 SGT*

# **A computational study on porosity evolution in parts produced by selective laser melting**

J. L. Tan<sup>a,b</sup>, C. Tang<sup>a</sup>, and C. H. Wong<sup>a,\*</sup>

<sup>a</sup> Singapore Centre for 3D Printing, School of Mechanical and Aerospace Engineering, Nanyang Technological University, 50 Nanyang Avenue, Singapore 639798

<sup>b</sup> SLM Solutions Singapore Pte. Ltd., 25 International Business Park, #02-15/17 German Centre, Singapore 609916

\*E-mail address: CHWong@ntu.edu.sg (C. H. Wong), Tel: (+65) 6790 5915 / 6790 4349

## **Abstract**

Selective Laser Melting (SLM) is a powder-bed additive manufacturing process that uses laser to melt powders, layer by layer to generate a functional 3D part. There are many different parameters, such as laser power, scanning speed and layer thickness, which play a role in determining the quality of the printed part. These parameters contribute to the energy density applied on the powder bed. Defects arise when insufficient or excess energy density is applied. A common defect in these cases is the presence of porosity. This paper studies the formation of porosities when inappropriate energy densities are used. A computational model was developed to simulate the melting and solidification process of SS316L powders in the SLM process. Three different sets of process parameters were used to produce 800  $\mu\text{m}$  long melt tracks and the characteristics of the porosities were analyzed. It was found that when low energy density parameters were used, the pores were found to be irregular in shapes and were located near the top surface of the powder bed. However, when high energy density parameters were used, the pores were either elliptical or spherical in shapes and were usually located near the bottom of the keyholes.

**Keywords:** Selective laser melting; modelling; porosity; keyhole; lack of fusion; solidification

## 1. Introduction

Additive Manufacturing (AM) has seen a surge of interest in the recent years [1]. It possesses certain characteristics which gives it an edge over conventional manufacturing methods. For instance, AM is able to cut down on material wastages by using only the required amount of raw materials. Another advantage of AM is design freedom. Instead of manufacturing multiple components and assembling them, AM allows user to print the part as a single-body unit [2]. Furthermore, it is difficult to produce part with complex geometries using conventional manufacturing. However, with AM, intricate design can be produced with relative ease [3]. An example is the use of lattice structures for weight reduction without compromising on the structural integrity of the part [4].

In Selective Laser Melting (SLM), several process parameters affect the quality of the printed parts. The energy density  $E$ , which is the applied energy per volume of material, is given by [5, 6, 7]

$$E = \frac{P}{v \cdot h \cdot L} \quad (1)$$

where  $P$  is the laser power,  $v$  is the laser scanning speed,  $h$  is the hatch spacing and  $L$  is the layer thickness. Based on Equation (1), it can be deduced that the energy density is a function of these four parameters. However, apart from these parameters, there are other factors which can affect the quality of the fabricated parts. For instance, the powder size distributions will affect the packing density of the powder bed layer whereas the laser spot size will affect the intensity of the laser [8, 9]. Using a wider distribution of powder sizes has shown to give a denser part compared to when using a narrower powder size distribution [10]. Increasing the laser spot size will lead to a decrease in energy intensity since the laser power will cover a bigger area of the

powder bed and this may result in incomplete melting of the powders. As such, the quality of the part is dependent on many different parameter combinations. Read et al. conducted a series of experiments using 4 parameters with 5 different values each [11]. Therefore, a total of 625 runs were conducted to test every possible combination without any additional samples to test for repeatability. This shows that relying solely on experiments to determine the optimum process parameters is not only time consuming but also expensive.

The use of simulation and modelling is a viable approach in tackling this obstacle. There are a variety of modelling techniques used to simulate the SLM process. Fu and Guo used Finite Element Analysis (FEA) to analyze the molten pool geometry [12]. While this model provided the molten pool geometry from the temperature field, it treated the powder layer as a continuous medium even though the powders behave in a granular manner in the actual SLM process. Tang et al. used Molecular Dynamics (MD) to investigate the SLM process in nano-scale [13]. In the simulation, the crystalline structures of the melted particles were analyzed. However, the scale of the model may not accurately represent the SLM process which is in micron-scale.

In the SLM process, defects can arise when the energy density applied is not optimum. A phenomenon known as balling occurs when insufficient energy density was used resulting in discontinuous tracks [14]. Balling effects can be overcome by applying high energy density such as using high laser power with low scanning speed [15]. Another defect commonly found in parts produced by SLM is porosity. Porosity can be formed from trapped gases in the melt pool at slow scanning speed or due to keyhole instability during rapid solidification of the metal leading to the collapse of the keyhole [16]. Since porosity is embedded within the part, it is difficult to detect as opposed to balling. These defects will result in parts with lower mechanical properties [17]. Non-destructive Testing (NDT) methods such as radiography can be used to monitor the

quality of the printed part [18]. Experiments revealed that porosity can be controlled by using suitable energy density and modifying the parameters in Equation 1 if required [19, 20].

Many experimental studies reported the development of porosity in parts fabricated by the SLM process. For instance, Aboulkhair et al. [16] observed near-spherical and irregular shaped pores in AlSi10Mg parts. The type of pores formed during SLM process is closely related with the scanning speed. Spherical pores are likely to be formed with lower speeds, whereas irregular pores are generated with high scanning velocities. They found numerous spherical pores at very low laser scanning speed. The number of spherical pores decreases as the speed increases until a certain range where pores are not formed. At scanning speeds above that range, irregular pores begin to form. Similar results were also reported by Garibaldi et al. [21] and Kaspeovich et al. [22]. Their results suggested the correlation between laser energy input and porosity formation in the selective laser melted samples. A high energy input can generate spherical pores, while low energy can create elongated and irregular defects. All these studies suggested the types of porosities are affected by processing conditions. Nevertheless, mechanisms of porosity development during SLM process have not been fully understood.

Powder bed fusion is a complex multi-physics process due to the heat transfer, fluid flow and complex geometries [23, 24]. A suitable physics-based model will therefore aid in understanding certain phenomena which occurs in SLM and how the selection of parameters will influence the quality of the printed part. This work investigates the formation of pores in the SLM process by varying the energy density applied on the powder bed by using a physics-based model. Observation of the development of the pores can provide insights on how the energy densities will affect the shape of the porosity.

## 2. Computational Model and Methodology

Using discrete element method (DEM), SS316L powders were first modeled and deposited onto a  $200 \times 1000 \mu\text{m}$  substrate surface of similar material properties using LIGGGHITS® (LAMMPS Improved for General Granular and Granular Heat Transfer Simulations) software [25]. The shapes of the powders are set to be spherical and their sizes follow a Gaussian distribution with mean diameter of  $27 \mu\text{m}$  and a full width at half maximum value of  $5 \mu\text{m}$ . Every powder's radii and coordinates were then exported to OpenFOAM® (Open Field Operation and Manipulation) software to generate the powders and their location on the substrate, and to perform computational fluid dynamics (CFD) simulation work. The time-step was set at  $10 \text{ ns}$  and a Cartesian mesh grid size of  $2.5 \mu\text{m}$  was used. A laser beam diameter of  $54 \mu\text{m}$  and layer thickness of  $27 \mu\text{m}$  were used for the simulations. A single track of  $800 \mu\text{m}$  in length was scanned for each of the three sets of parameters used for this study. The initial temperatures of the powders and substrate were set to  $300 \text{ K}$  and the boundary conditions were assumed to be adiabatic.

### 2.1 Heat transfer and fluid flow

In the model, metallic and gas phases were used to show the evolution of the interface during the melting and solidification process in SLM. To capture the metal and gas interface, the Volume of Fluid (VOF) method was adopted. In the model, a function was used to determine the metallic and gaseous phase  $\alpha_1$  and  $\alpha_2$  respectively. The relationship between these phases can be defined as [26]

$$\alpha_1 + \alpha_2 = 1 \quad (1)$$

When  $\alpha_1 = 1$ , the mesh consists of only metallic phase. Likewise, when  $\alpha_2 = 1$ , the mesh consists of solely gas. When the solid metal powders experience melting, it will change from solid to liquid state. This change in phase is described using the liquid fraction  $\gamma$ . It follows a linear function ranging from zero to one, where the value of zero means the metal is completely solid while the value of one means the metal is fully liquid [27]. When  $\gamma$  is between zero and one, the metal is in a mushy state.

The molten metal was assumed to be an incompressible fluid. This means that for a selected volume, the amount of fluid entering it is equal to the amount of fluid exiting. Hence, the continuity equation expressing the conservation of mass can be written as

$$\nabla \cdot \vec{u} = 0 \quad (2)$$

where  $\vec{u}$  is the flow velocity. The forces acting on the system during the SLM process were considered in the Navier-Stokes or the conservation of momentum equation. Equation (3) shows the pressure forces on the left hand side being driven by the external forces on the right hand side of the equation, giving

$$\begin{aligned} \frac{\partial \bar{\rho} \vec{u}}{\partial t} + \nabla \cdot (\bar{\rho} \vec{u} \otimes \vec{u}) = & -\nabla p + \nabla \cdot (\bar{\mu} \cdot \nabla \vec{u}) + \bar{\rho} g \vec{e}_z \beta (T - T_{ref}) - K_c \left[ \frac{(1 - f_l)^2}{f_l^3 + C_k} \right] \vec{u} \\ & + \left\{ \sigma \kappa h + \frac{d\sigma}{dT} [\nabla T - h(h \cdot \nabla T)] + p_v \right\} |\alpha_1| \frac{2\bar{\rho}}{(\rho_{metal} + \rho_{air})} \end{aligned} \quad (3)$$

where  $\bar{\rho}$  is the density,  $\rho_{metal}$  is the density of the metal,  $\rho_{air}$  is the density of air,  $t$  is the time,  $\bar{\mu}$  is the viscosity,  $T$  is the temperature,  $T_{ref}$  is the reference temperature,  $p$  is the pressure,  $g$  is the gravitational acceleration,  $p_v$  is the recoil pressure,  $\vec{e}_z$  is the unit normal to the gravitational

force,  $\beta$  is the thermal expansion coefficient,  $K_c$  is the permeability coefficient,  $f_l$  is the fraction of liquid metal,  $C_k$  is a constant,  $\sigma$  is the surface tension, and  $\kappa$  is the surface curve at unit normal to  $\hat{n}$ .

$K_c \left[ \frac{(1-f_l)^2}{f_l^3 + C_k} \right] \mu$  is the Carman-Kozeny equation derived from the Darcy's Law [28]. It describes the flow in the mushy region of the molten pool. The constant  $C_k$  was introduced to avoid division by zero and was set to be a small value.

$\frac{d\sigma}{dT} [\nabla T - \hat{n}(\hat{n} \cdot \nabla T)]$  describes the Marangoni force or thermo-capillary force that varies with temperature. The Marangoni force occurs due to the different surface tension between two phases at the interface. Studies have shown that it strongly affects the flow pattern in a melt pool [29].

In laser melting process, the temperature within the laser beam will exceed the boiling point of the material. In such a situation, the metal will vaporize and exert a pressure known as recoil pressure  $p_v$  on the surface of the molten pool. This will form a depression at the leading edge of the melt track. The equation for recoil pressure is given by [30]

$$p_v = 0.54 p_0 \exp \left( \Delta H_{LV} \frac{T - T_{LV}}{RTT_{LV}} \right) \quad (4)$$

where  $p_0$  is the atmospheric pressure,  $\Delta H_{LV}$  is the latent heat of vaporization,  $R$  is the universal gas constant, and  $T_{LV}$  is the boiling temperature at atmospheric pressure.



In the system, there are energy input from the laser source as well as the heat losses due to conduction, convection and radiation. Change in phase (solid to liquid) of the metal during melting will require energy from the system, known as the latent heat of fusion. These processes are included in the conservation of energy equation given by

$$\frac{\partial \bar{\rho} \bar{C}_p T}{\partial t} + \nabla \cdot (\bar{\rho} \bar{u} \bar{C}_p T) = - \frac{\partial \bar{\rho} \Delta H_f}{\partial t} - \nabla \cdot (\bar{\rho} \bar{u} \Delta H_f) + \nabla \cdot (\bar{k} \nabla T) - \left[ h_c (T - T_{ref}) + \sigma_s \varepsilon (T^4 - T_{ref}^4) + Q_v \right] |\alpha_1| \frac{2 \bar{C}_p \bar{\rho}}{C_{p-metal} \rho_{metal} + C_{p-air} \rho_{air}} + Q_T \quad (5)$$

where  $C_{p-metal}$  is the specific heat of the metal,  $C_{p-air}$  is the specific heat of air,  $\bar{C}_p$  is the specific heat,  $\Delta H_f$  is the enthalpy change due to fusion,  $\bar{k}$  is the thermal conductivity,  $h_c$  is the heat transfer coefficient,  $\sigma_s$  is the Stefan-Boltzmann constant,  $\varepsilon$  is the emissivity,  $Q_v$  is the heat loss due to evaporation, and  $Q_T$  is the heat input.

The heat loss due to conduction, convection and radiation are given by  $\nabla \cdot (\bar{k} \nabla T)$ ,  $h_c (T - T_{ref})$  and  $\sigma_s \varepsilon (T^4 - T_{ref}^4)$  respectively.

Due to the high temperature of the molten metal during the melting process, surface evaporation at the molten pool may arise. This will result in loss of energy to convert the metal from liquid to gaseous phase and is expressed as

$$Q_v = 0.82 \frac{\Delta H_v}{\sqrt{2\pi MRT}} p_0 \exp \left( \Delta H_v \frac{T - T_{LV}}{RT T_{LV}} \right) \quad (6)$$

where  $M$  is the molar mass and  $\Delta H_v$  is the enthalpy of vaporization of the metal.

The heat source used in this work follows the Gaussian distribution and is given by

$$Q_T = \frac{2\eta P}{\pi r^2} \exp\left(-2 \frac{x^2 + y^2}{r^2}\right) \quad (7)$$

where  $P$  is the laser power,  $r$  is the laser beam radius,  $x$  and  $y$  are the cartesian coordinates of the center of the laser beam, and  $\eta$  is the absorptivity of the powder bed and is taken to be 0.35.

## 2.2 Material Properties

The material used for the simulations is SS316L. The material properties, coefficients and constants are listed in Table 1. In the simulation, the material's properties are temperature dependent that provides a better representation of the properties of the mushy region.

The density of metal in the mushy state is given by

$$\rho_{metal} = \gamma(\rho_{liquid} + 0.0393T + 0.00018T^2) + (1 - \gamma)(\rho_{solid} - 0.4209T - 3.984 \times 10^{-5}T^2) \quad (8)$$

where  $\rho_{liquid}$  is the base value for the density of the metal in liquid state and  $\rho_{solid}$  is the base value for the density of the metal in solid state.

The thermal conductivity of the metal is given by

$$\lambda_{metal} = \gamma(\lambda_{liquid} + 0.003279T) + (1 - \gamma)(\lambda_{solid} - 0.1571T) \quad (9)$$

where  $\lambda_{liquid}$  is the base value for the density of the metal in liquid state and  $\lambda_{solid}$  is the base value for the density of the metal in solid state.

To calculate the properties of a single mesh, the generic equation computed as

$$\phi = \phi_{air} \alpha_2 + \phi_{metal} \alpha_1 \quad (10)$$

can be used where  $\phi_{air}$  is the selected material property of the gas and  $\phi_{metal}$  is the selected property of the metal. Therefore, the thermal conductivity of the mesh is  $\lambda_{air}\alpha_2 + \lambda_{metal}\alpha_1$ .

### 3. Results and discussion

#### 3.1 Single track formation during SLM

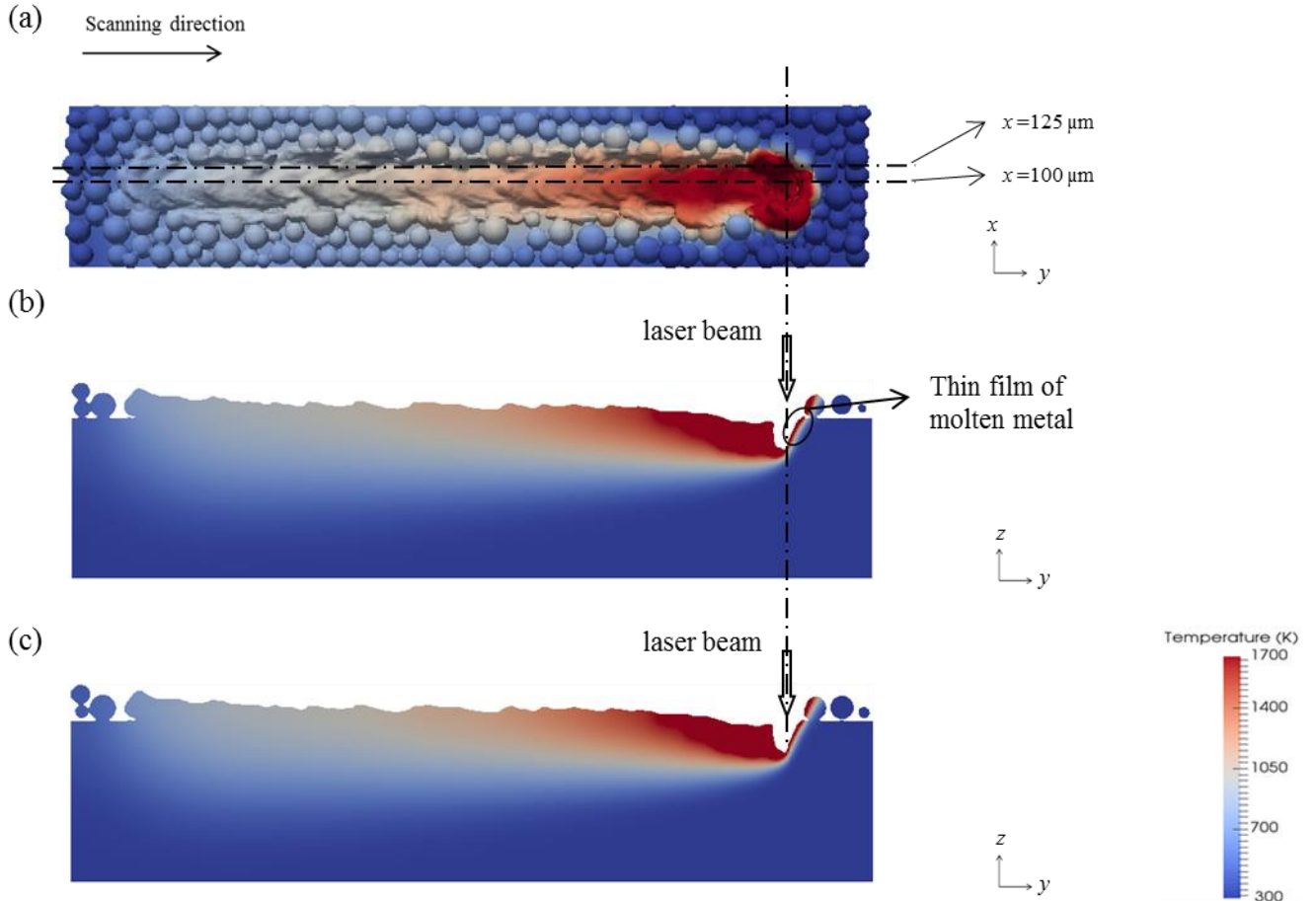


Fig. 1 Melt track using  $P = 200 \text{ W}$ ,  $v = 1.5 \text{ m/s}$  (a) Top view, sliced at (b)  $x = 100 \mu\text{m}$ , and (c)  $x = 125 \mu\text{m}$ .

Using a scanning speed of  $1.5 \text{ m/s}$  and laser power of  $200 \text{ W}$ , the evolution of temperature field and geometry of the melt track are shown in Fig. 1. It can be clearly seen that a continuous and

relatively smooth track is formed due to the fusion of metal particles. As shown in Fig. 1, metal particles near and within the laser beam spot were irradiated, heated up and melted. Due to the surface tension force, those melted particles immediately coalesce with nearby powders and the substrate, leading to the formation of a track. In addition, an obvious depression zone, attributed to the recoil pressure, can be observed near the laser beam spot. The metal at the center of the laser beam will reach temperatures above its boiling point leading to evaporation of the metal. This metal vapour exerts a force which results in the depression observed at the leading edge of the melt pool. Such phenomenon is in agreement with previous experimental study [31]. The local temperature quickly drops as the laser beam moves away and this results in a drop in evaporation rate of the metal. This leads to a rapid decrease of the recoil pressure force. In this situation, the surface tension starts to dominate the dynamics of fluids, resulting in the motion of fluid towards the center of the depression zone. The reverse motion of liquid melts causes the collapse (or recovery) of the depression zone. The keyhole maintains its profile when the recoil pressure balances with the surface tension as shown in experiments, giving a constant depth throughout the scanning process [31]. As illustrated in Fig. 1(b), a thin liquid layer can be observed in the front of the depression zone, which is consistent with previous study [32]. Moreover, the keyhole depression at the end of the track retains its shape despite after the heat source is turned off and is attributed to the fast cooling and solidification near the depression zone. Similar observation has also been reported by laser welding experiments where Eriksson et al. studied the inclination of the keyhole front [33]. One may also find such characteristics in SLM experiments [34] and it was reported that a depression zone is formed at the end of the melt track.

The longitudinal 2D slices of the model in Figs. 1(b) and (c) are employed to determine whether any porosity is formed after the laser scanning. Similar operation has been conducted by SLM experiments to show the distribution of porosity [26]. In Figs. 1(b) and (c), the cross-sectional slices were taken at  $x = 100 \mu\text{m}$  (corresponding to the center of the laser beam) and  $x = 125 \mu\text{m}$  (near the inside edge of the laser beam), respectively. Since  $x = 125 \mu\text{m}$  falls within the region covered by the laser beam spot, full melting of the powders should be observed when sufficient energy density is applied. This corresponds to experiments where the track widths of a continuous single track are larger than the diameter of the laser spot [35, 36]. As shown in Figs. 1, no porosity could be observed below the solidified track, indicating the applied laser parameters are suitable in preventing the development of porosities. Additionally, Figs. 1(b) and (c) provide information about the surface roughness of the solidified track. The track is relative smooth as shown in the figures. As discussed by Zhou et al. [37], a smooth surface is significant in eliminating interlayer porosities from building up in the next layer. On the contrary, a rough surface will affect the powder distribution across the layer and deteriorates laser absorptivity.

### **3.2 Formation of irregular pores**

Irregular pores are often observed in experiments when using parameters of lower energy densities (high scanning speed and/or low laser power) than the optimal values [16, 38]. At high scanning speed, balling effects occurs and gives rise to discontinuous tracks and pores trapped between these balls [39]. In the subsequent layers, the molten metal flow is disturbed due to the unevenness of the preceding layer and is unable to fill up the pores left behind from the previous layers. To simulate porosity from the lack of energy density, a low laser power of 75 W was adopted. The scanning speed was retained at 1.5 m/s, thus reducing the total energy density by more than two times according to Equation (1).

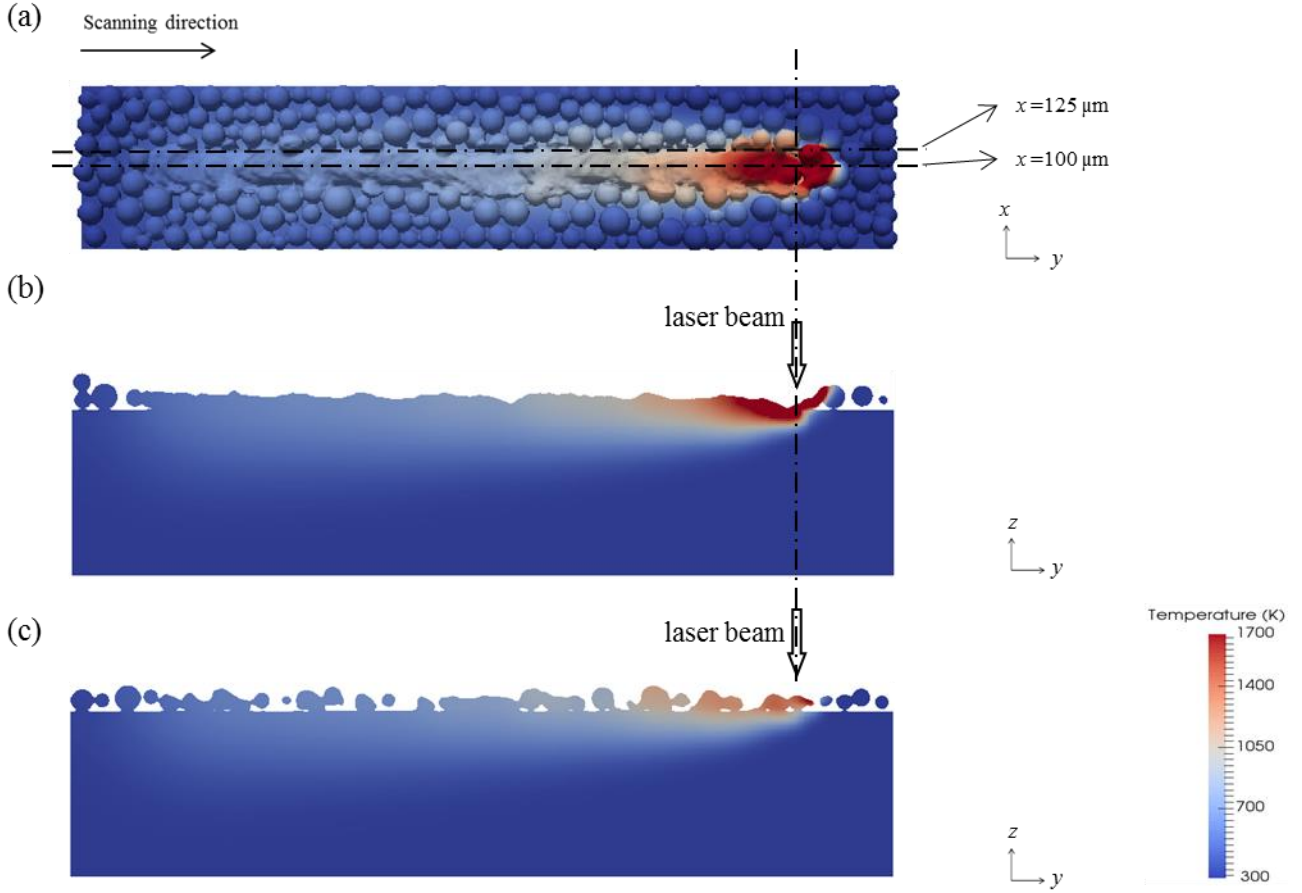


Fig. 2 Melt pool track using low laser power,  $P = 75 \text{ W}$ ,  $v = 1.5 \text{ m/s}$  (a) top view, sliced at (b)  $x = 100 \mu\text{m}$ , and (c)  $x = 125 \mu\text{m}$ .

In Fig. 2(a), it was observed that the track width is narrower than that in Fig. 1(a). Lower laser power will produce a smaller melt pool since lesser energy was used to melt the powders. This can be seen in Fig. 2(b) where the molten track has a shallower depth than that in Fig. 1(b). In Fig 2(c), it was also observed that the powders that are within the laser beam diameter did not experience full melting that contributes to a smaller molten pool. With a smaller molten pool, there is insufficient molten metal to flow and fill up the gaps between the powders. Therefore,

pores are formed and will take on irregular shapes from these gaps as seen in Fig. 2(c). These are similar to experimental results reported in Aboulkhair's et al. work [16]. Since the powders were poorly melted, they will not adequately fuse with the substrate. This will result in poor interlayer bonding leading to delamination defects seen in experiments with low energy density parameters [40].

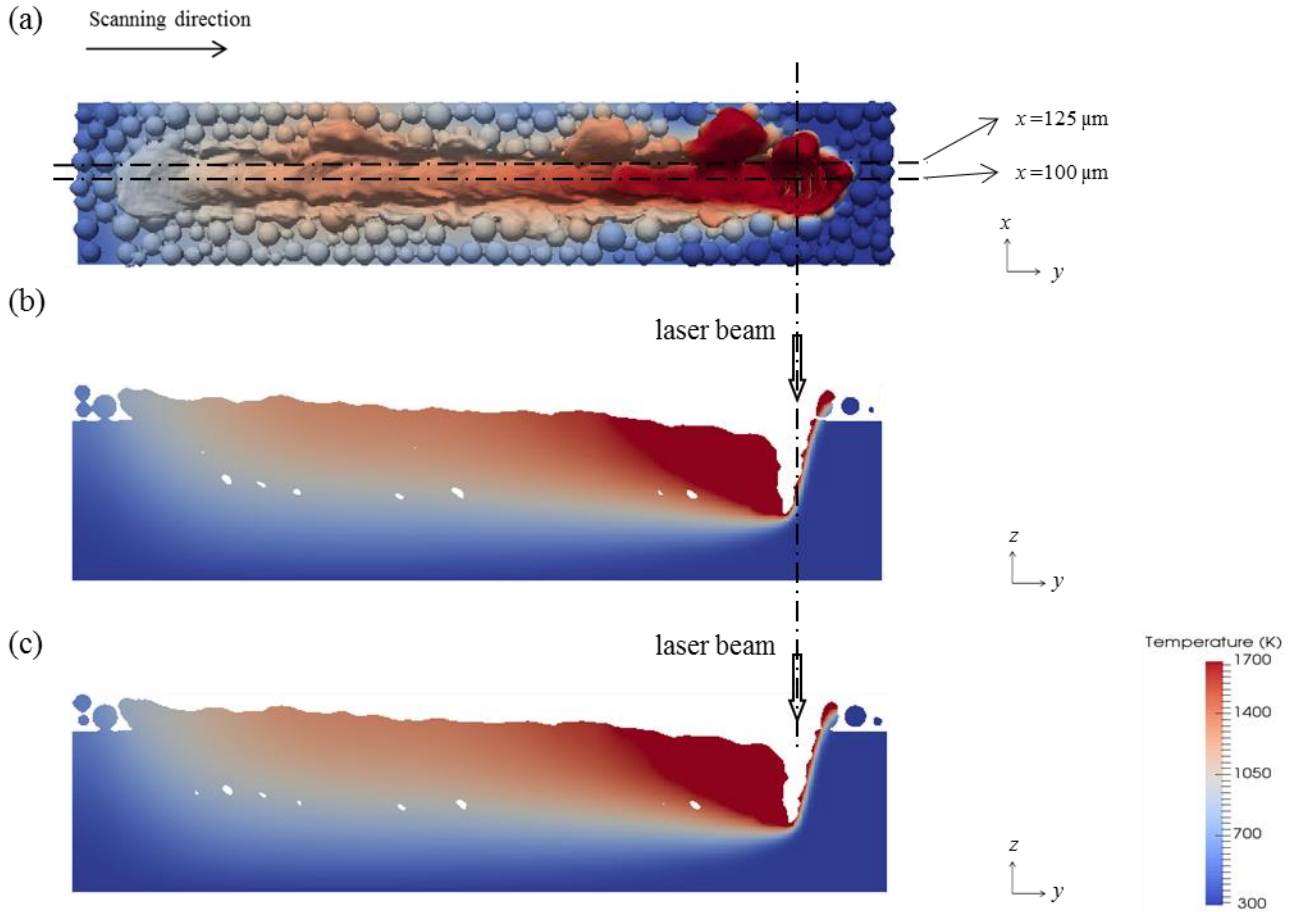
Additionally, the melt pool depth was measured to be 10  $\mu\text{m}$  which is less than the layer thickness of the simulation. For the laser to remelt the layer directly beneath the current layer, the melt pool depth will have to be more than the layer thickness. When a new layer of powders is deposited, the laser will therefore not be able to completely melt the layer beneath it. With insufficient melting, there will not be enough molten metal to fill up the porosities from the previous layer. Hence, the shapes and positions of these porosities due to the lack of fusion are unaffected by the scanning process of the subsequent layers.

### **3.3 Formation of spherical pores**

Previous experiments reported that low scanning speed and high laser energy input result in the formation of porosities [41]. Therefore, a high laser power of 400 W and the same scanning speed of 1.5 m/s were employed to study the formation of pores.

Experiments using SLM reported findings that using energy density above the optimal range will produce parts with increased porosities [16]. With higher energy density applied on the powder bed, the temperature of the melt pool will increase that leads to more vaporized metal and increased recoil pressure. These result in deeper and unstable keyhole being formed [42]. Due to its instability, the keyhole will collapse, trapping gas within the melt pool. The increase in recoil pressure also leads to more molten metal being pushed to the sides of the tracks as seen in Fig.

271 3(a). Increasing the energy density will lead to an increase in the keyhole depth as seen in Figs.  
 272 3(b) and (c) when compared to that in Figs. 1(b) and (c).



274 Fig. 3 Melt pool track using high laser power,  $P = 400 \text{ W}$ ,  $v = 1.5 \text{ m/s}$  (a) top view, sliced at (b)  
 275  $x = 100 \mu\text{m}$ , and (c)  $x = 125 \mu\text{m}$ .

276  
 277 In Fig. 4, the formation of the pores can be studied. As the keyhole travels along the scanning  
 278 direction, the molten metal tailing it will attempt to fill up the vacancy. Due to convection, the  
 279 molten metal at Region A will flow away from the keyhole shown by its resultant velocity  
 280 vector. At the same time, the molten metal in Region B will collapse inwards towards the



keyhole due to surface tension. With the bottom and top of the molten metal having different flow directions, the molten metal will enclose and trap the gas within the keyhole. This gas consists mainly the metal vapour trying to escape from the bottom of the keyhole [42]. The cross-section along the track's length showed similar characteristics when compared with experiments by King et al. [41]. The majority of the keyhole porosities were located near the bottom of the keyhole as shown in Fig. 3(b) and (c). From Fig. 4, the velocities of the tailing end of the keyhole, in Region B, can reach up to 5 m/s. This rapid flow of the molten metal to fill the keyhole will give insufficient time for the gas to escape from the collapsing keyhole.

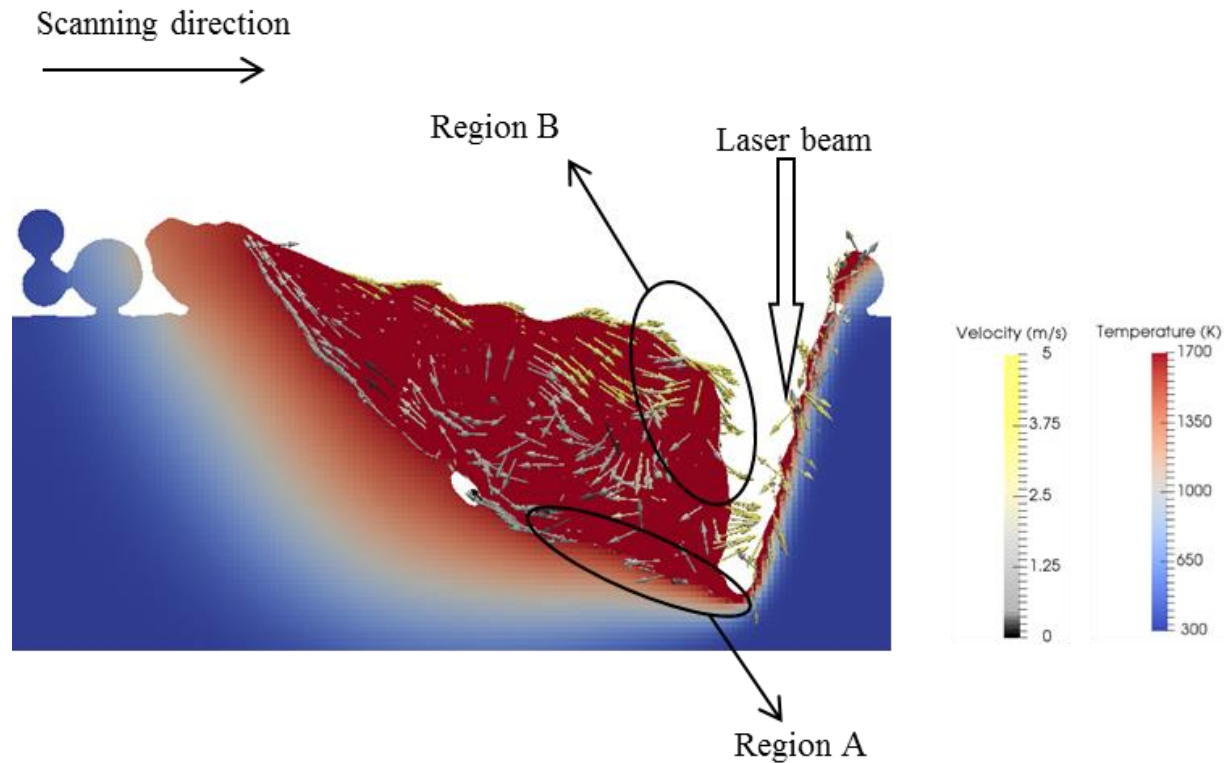


Fig. 4 Velocity vectors of molten metal around the keyhole at  $x = 100 \mu\text{m}$ .

292 Fig. 5 shows the cross-sections of the melt pool in the  $x$ -axis using laser power of 400 W and  
293 scanning speed of 1.5 m/s. The formation of a pore was observed from the time when the  
294 keyhole began to collapse until the time when the molten metal trapped the gas bubble. In Fig.  
295 5(a), the molten metal near the surface is flowing rapidly to fill up the keyhole. However, the  
296 molten metal near the base of the keyhole was flowing away from the keyhole as seen in Region  
297 A of Fig. 4. This leads to gas being trapped as seen in Figs. 5(b) to (c). Within the molten metal,  
298 the trapped gas will take on an elliptical or spherical shape due to the effects of surface tension as  
299 seen in Fig. 5(d). Due to surface tension, the molten metal will be pulled towards each other,  
300 minimizing the surface area of the liquid-gas interface. These corresponds to experimental  
301 results reported by King et al. [41].

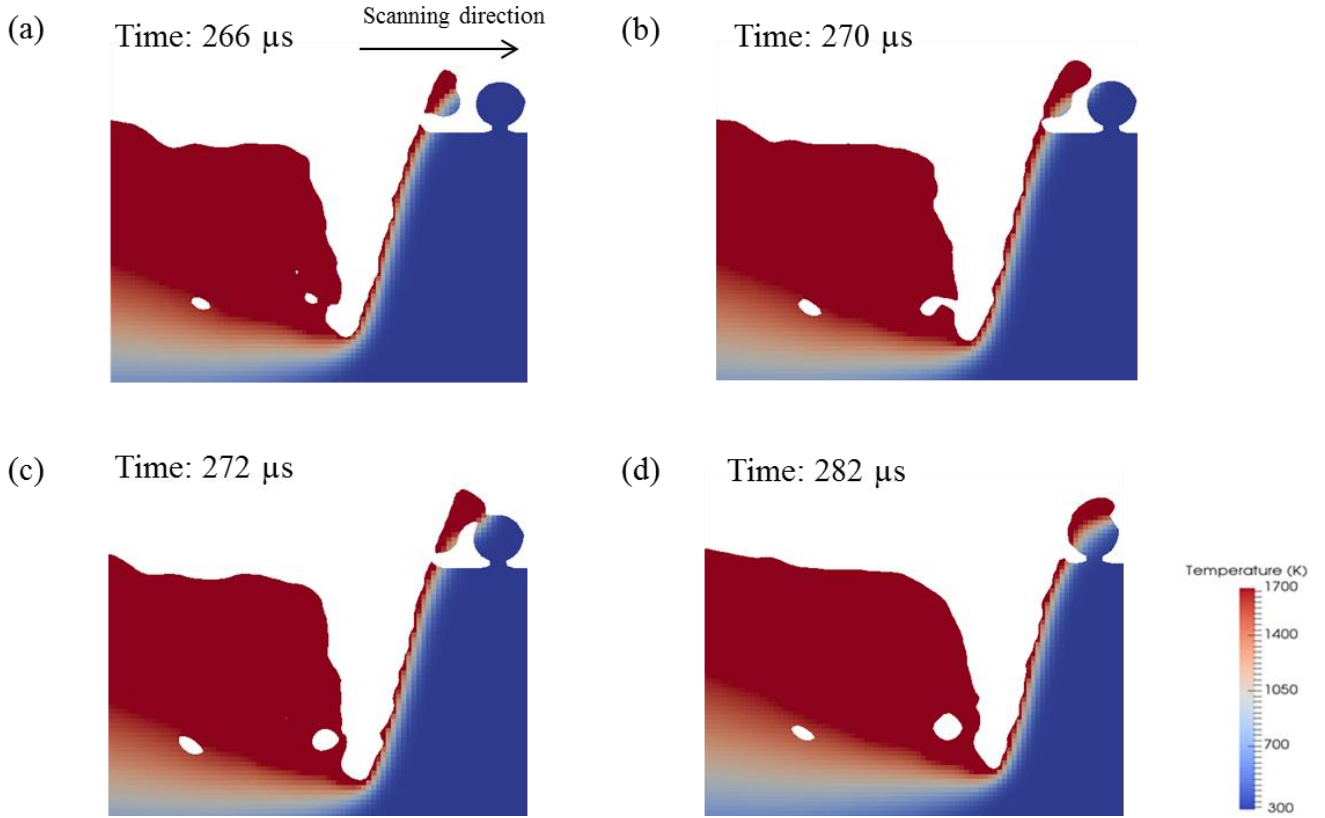


Fig. 5 Cross-section of powder bed at  $x = 95 \mu\text{m}$  showing evolution of a keyhole porosity in the molten metal starting with (a) the unstable keyhole beginning to collapse at time = 266  $\mu\text{s}$ , (b) trapping of gas within the molten metal at time = 270  $\mu\text{s}$ , (c) molten metal enclosing the gas forming pores at time = 272  $\mu\text{s}$ , and (d) spherical pores formed due to surface tension at time = 282  $\mu\text{s}$ .

The keyhole depth of 120  $\mu\text{m}$  exceeds the layer thickness of 27  $\mu\text{m}$ . Therefore, in the subsequent layers, the keyhole will be able to reach the existing pores due to the deep penetration depth of the laser. This will remelt the metal from the previous layer(s) and remove any existing pores that are within reach of the keyhole. However, the keyhole is unstable and will result in the

formation of new keyhole pores. Therefore, the keyhole porosities may change their sizes and locations after the scanning of every layer.

#### **4. Conclusions**

Different energy density parameters were studied to observe the effects they have on pore formation. The parameters using laser power of 200 W and scanning speed of 1.5 m/s were chosen as a reference for comparisons. Energy densities lower and higher than this reference were used in the simulations to study the differences between the pores formed in each scenario. Pores were formed when using too low or too high energy density parameters. In the reference parameters, sufficient energy was used to melt the metal powders and the keyhole remained stable with no pores observed. However, when low scanning speed was used, the pores were formed due to the incomplete melting of the powders, leaving gaps between the partially melted powders.

Similarly, pores were formed when high energy density parameters were used. The collapse of the unstable keyhole was due to the high velocities of the molten metal near the surface flowing back to fill up the keyhole while the molten metal near the base of the keyhole was flowing away from the keyhole because of the recoil pressure. The flow velocity and direction of the molten metal can be shown using this simulation to explain the formation of keyhole porosities. The gas near the bottom are more likely to be trapped from the collapsing keyhole. Therefore, most of the keyhole porosities are formed near the base of the keyhole. The shapes of these pores take on an elliptical or spherical shape due to the effect of surface tension.

This physics-based model has given a clearer understanding of the formation of pores during the melting and solidification process. This paper established that the porosities' characteristics vary

335 when using different parameters. It also provides an illustration and explanation on the  
336 mechanics behind the formation of keyhole porosity.

337

338    **Acknowledgement**

339    This project is funded under the Economic Development Board – Industrial Postgraduate  
340    Programme (EDB-IPP), in conjunction with Singapore Centre for 3D Printing and SLM  
341    Solutions Singapore Pte Ltd.

342    **Author Disclosure Statement**

343    No competing financial interests exists.

- [1] W. Gao, Y. Zhang, D. Ramanujan, K. Ramani, Y. Chen, C. B. Williams, C. Wang, Y. Shin, S. Zhang and P. Zavattieri: *Computer-Aided Design*, 2015, vol. 69, pp. 65-89.
- [2] I. Gibson, D. W. Rosen and B. Stucker: *Additive manufacturing technologies* (Vol. 238), Springer, New York, 2010.
- [3] K. K. Wong, J. Y. Ho, K. C. Leong and T. N. Wong: *Virtual and Physical Prototyping*, 2016, no. 3, vol. 11, pp. 159-165.
- [4] C. K. Chua, C. H. Wong and W. Y. Yeong: *Standards, Quality Control, and Measurement Sciences in 3D Printing and Additive Manufacturing*, Academic Press, USA, 2017.
- [5] L. Thijs, F. Verhaeghe, T. Craeghs, J. Humbeeck and J. Kruth: *Acta Materialia*, 2010, no. 9, vol 58, pp. 3303-3312.
- [6] D. K. Do and P. Li: *Virtual and Physical Prototyping*, 2016, no. 3, vol. 11, pp. 41-47.
- [7] C. Y. Yap, C. K. Chua and Z. L. Dong: *Virtual and Physical Prototyping*, 2016, no. 1, vol. 11, pp. 21-26.
- [8] I. Yadroitsev, P. Bertrand and I. Smurov: *Applied Surface Science*, 2007, no. 19 vol. 253, pp. 8064-8069.
- [9] A. T. Sutton, C. S. Kriewall, M. C. Leu and J. W. Newkirk: *Virtual and Physical Prototyping*, 2017, no. 1, vol. 12, pp. 3-29.
- [10] B. Liu, R. Wildman, C. Tuck, I. Ashcroft and R. Hague: in *Solid Freeform Fabrication Symposium*,

2011, Austin, Texas.

- [11] N. Read, W. Wang, K. Essa and M. Attallah: *Materials & Design*, 2015, vol. 65, pp. 417-424.
- [12] C. H. Fu and Y. B. Guo: *3-Dimensional Finite Element 25th Annual International Solid Freeform Fabrication Symposium*, 2014.
- [13] C. Tang, B. Li and C. H. Wong: *1st International Conference on Progress in Additive Manufacturing*, Singapore, 2014.
- [14] D. Gu and Y. Shen: *Journal of Alloys and Compounds*, 2007, no. 1-2, vol. 432, pp. 136-166.
- [15] R. Li, J. Liu, Y. Shi, L. Wang and W. Jiang: *The International Journal of Advanced Manufacturing Technology*, 2011, no. 9-12, vol. 59, pp. 1025-1035.
- [16] N. Aboulkhair, N. Everitt, I. Ashcroft and C. Tuck: *Additive Manufacturing*, 2014, vols. 1-4, pp. 77-86.
- [17] J. Kruth, L. Froyen, J. V. Vaerenbergh, P. Mercelis, M. Rombouts and B. Lauwers: *Journal of Materials Processing Technology*, 2004, no. 1-3, vol. 149, pp. 616-622.
- [18] Q. Y. Lu and C. H. Wong: *Virtual and Physical Prototyping*, 2017, no. 4, vol. 12, pp. 301-321.
- [19] K. Monroy, J. Delgado and J. Ciurana: *Procedia Engineering*, 2013, vol. 63, pp. 361-369.
- [20] M. Gan and C. H. Wong: *Journal of the European Ceramic Society*, 2017, no. 13, vol. 37, pp. 4147-4154.
- [21] M. Garibaldi, I. Ashcroft, M. Simonelli and R. Hague: *Acta Materialia*, 2016, vol. 110, pp. 207-216.



- [22] G. Kasperovich and J. Hausmann: *Journal of Materials Processing Technology*, 2015, vol. 220, pp. 202-214.
- [23] A. Simchi: *Materials Science and Engineering: A*, 2006, no. 1-2, vol. 428, pp. 148-158.
- [24] M. Brandt, *Laser Additive Manufacturing: Materials, Design, Technologies, and Applications*, Woodhead Publishing, 2016.
- [25] Cfdem.com: LIGGGHTS Open Source Discrete Element Method Particle Simulation Code | CFDEM®project, 2017. [Online]. Available: <https://www.cfdem.com/liggghts-open-source-discrete-element-method-particle-simulation-code>.
- [26] C. Qiu, C. Panwisawas, M. Ward, H. Basoalto, J. Brooks and M. Attallah: *Acta Materialia*, 2015, vol. 96, pp. 72-79.
- [27] F. Rösler and D. Brüggemann: *Heat and Mass Transfer*, 2011, no. 8, vol. 47, pp. 1027-1033.
- [28] V. R. Voller and C. Prakash: *International Journal of Heat and Mass Transfer*, 1987, no. 8, vol. 30, pp. 1709-1719.
- [29] Z. Gałązka and H. Wilke: *Journal of Crystal Growth*, 2000, no. 1-4, vol. 216, pp. 389-398.
- [30] J. Cho, D. Farson, J. Milewski and K. Hollis: *Journal of Physics D: Applied Physics*, 2009, no. 17, vol. 42, p. 175502.
- [31] S. Fujinaga, H. Takenaka, T. Narikiyo, S. Katayama and A. Matsunawa: *Journal of Physics D: Applied Physics*, 2000, no. 5, vol. 33, pp. 492-497.

- [32] S. A. Khairallah, A. T. Anderson, A. Rubenchik and W. E. King: *Acta Materialia*, 2016, vol. 108, pp. 36-45.
- [33] I. Eriksson, J. Powell and A. Kaplan: *Optics and Lasers in Engineering*, 2013, no. 6, vol. 51, pp. 735-740.
- [34] J. Trapp, A. M. Rubenchik, G. Guss and M. J. Matthews: *Applied Materials Today*, 2017, vol. 9, pp. 341-349.
- [35] I. Yadroitsev, A. Gusarov, I. Yadroitsava and I. Smurov: *Journal of Materials Processing Technology*, 2010, no. 12, vol. 210, pp. 1624-1631.
- [36] I. Yadroitsev, P. Krakhmalev, I. Yadroitsava, S. Johansson and I. Smurov: *Journal of Materials Processing Technology*, 2013, no. 4, vol. 213, pp. 606-613.
- [37] X. Zhou, X. Liu, D. Zhang, Z. Shen and W. Liu: *Journal of Materials Processing Technology*, 2015, vol. 222, pp. 33-42.
- [38] D. Gu, Y. Hagedorn, W. Meiners, G. Meng, R. Batista, K. Wissenbach and R. Poprawe: *Acta Materialia*, 2012, no. 9, vol. 60, pp. 3849-3860.
- [39] R. Li, J. Liu, Y. Shi, L. Wang and W. Jiang: *The International Journal of Advanced Manufacturing Technology*, 2012, no. 9-12, vol. 59, pp. 1025-1035.
- [40] E. Louvis, P. Fox and C. J. Sutcliffe: *Journal of Materials Processing Technology*, 2011, no. 2, vol. 211, pp. 275-284.
- [41] W. E. King, H. D. Barth, V. M. Castillo, G. F. Gallegos, J. W. Gibbs, D. E. Hahn and A. M. Rubenchik:

Journal of Materials Processing Technology, 2014, no. 2, vol. 214, pp. 2915-2925.

- [42] A. Matsunawa, J. Kim, N. Seto, M. Mizutani and S. Katayama: Journal of Laser Applications, 1998, no. 6, vol. 10, pp. 247-254.

346

347

348 Table 1. Physical Properties for SS316L used in simulations.

Physical Properties	Values
Solidus temperature (K)	1658
Liquidus temperature (K)	1723
Boiling temperature (K)	3090
Surface tension ( $\text{N m}^{-1}$ )	1.6
Coefficient of surface tension ( $\text{N m}^{-1} \text{K}^{-1}$ )	$8 \times 10^{-4}$
Base thermal conductivity of solid ( $\text{W m}^{-1} \text{K}^{-1}$ )	9.248
Base thermal conductivity of liquid ( $\text{W m}^{-1} \text{K}^{-1}$ )	12.41
Reference temperature (K)	300
Base density of liquid ( $\text{kg m}^{-3}$ )	7433
Base density of solid ( $\text{kg m}^{-3}$ )	8084
Specific heat of solid metal ( $\text{J kg}^{-1} \text{K}^{-1}$ )	462
Specific heat of liquid metal ( $\text{J kg}^{-1} \text{K}^{-1}$ )	775
Latent heat of fusion ( $\text{J kg}^{-1}$ )	$2.7 \times 10^6$
Latent heat of vaporization ( $\text{J kg}^{-1}$ )	$7.45 \times 10^6$
Emissivity	0.26
Convective coefficient ( $\text{W m}^2 \text{K}$ )	80
Darcy term coefficient ( $\text{kg m}^{-3} \text{s}^{-1}$ )	$1 \times 10^6$
Stefan-Boltzmann's constant ( $\text{W m}^{-2} \text{K}^{-4}$ )	$5.67 \times 10^{-8}$
Universal gas constant ( $\text{J K}^{-1} \text{mol}^{-1}$ )	8.3144
Atmospheric pressure ( $\text{N m}^{-2}$ )	101000

Molar Mass ( $\text{kgmol}^{-1}$ )

0.05593

---

349

350

**Figure captions list**

Fig. 1 Melt track using  $P = 200$  W,  $v = 1.5$  m/s (a) Top view, sliced at (b)  $x = 100$   $\mu\text{m}$ , and (c)  $x = 125$   $\mu\text{m}$ .

Fig. 2 Melt pool track using low laser power,  $P = 75$  W,  $v = 1.5$  m/s (a) top view, sliced at (b)  $x = 100$   $\mu\text{m}$ , and (c)  $x = 125$   $\mu\text{m}$ .

Fig. 3 Melt pool track using high laser power,  $P = 400$  W,  $v = 1.5$  m/s (a) top view, sliced at (b)  $x = 100$   $\mu\text{m}$ , and (c)  $x = 125$   $\mu\text{m}$ .

Fig. 4 Velocity vectors of molten metal around the keyhole at  $x = 100$   $\mu\text{m}$ .

Fig. 5 Cross-section of powder bed at  $x = 95$   $\mu\text{m}$  showing evolution of a keyhole porosity in the molten metal starting with (a) the unstable keyhole beginning to collapse at time = 266  $\mu\text{s}$ , (b) trapping of gas within the molten metal at time = 270  $\mu\text{s}$ , (c) molten metal enclosing the gas forming pores at time = 272  $\mu\text{s}$ , and (d) spherical pores formed due to surface tension at time = 282  $\mu\text{s}$ .